Studies on Strongly Swirling Flows in the Full Space of a Volute Cyclone Separator

L. Y. Hu, L. X. Zhou, and J. Zhang
Dept. of Engineering Mechanics, Tsinghua University, Beijing 100084, China

M. X. Shi,
Institute of Chemical Engineering, Petroleum University, Changping, Beijing 102249, China

DOI 10.1002/aic.10354
Published online in Wiley InterScience (www.interscience.wiley.com).

The three-dimensional (3-D) strongly swirling turbulent flows in the full space of a volute cyclone separator was measured using laser Doppler velocimetry (LDV), and was simulated using an improved Reynolds stress equation model by modifying the empirical constants in the isotropization of production and convection model (IPCM) + wall pressure–strain term of the Reynolds stress equation, incorporated into the platform of FLUENT 6.0. Predicted Reynolds stress model (RSM) velocities are more reasonable than those obtained previously. The specific features of turbulent flows in the separation space, dust hopper, annular space, and the outlet tube are different. The results show that the time-averaged tangential velocity profiles in the separation space have a typical Rankine-vortex structure. In some regions, such as the entrance, the vicinity of the top of the annular space, the inner vortex-flow region, the vicinity of the discharge port, the vicinity of the wall, the intersection part between the upward and downward flows, the turbulent intensity is very large and changes sharply; the turbulence is anisotropic in most regions, but the magnitudes of three RSM velocity components are of the same order of magnitude. The distribution of time-averaged tangential velocity is asymmetric in the annular space. The longitudinal secondary vortexes exist near the top of the dust hopper and the top of the cyclone. The distribution of time-averaged axial velocity in the exit tube is entirely different from that in the separation space.
AIChE J, 51: 740–749, 2005
Keywords: volute cyclone separator, laser Doppler velocimetry (LDV), numerical simulation, turbulent flows

Introduction

Studies on the turbulent flow field in cyclones are needed for improving the cyclone performance. For experimental studies, previous studies are mainly related to time-averaged velocities, whereas the turbulence properties of 3-D strongly swirling flows are less reported. DeOtte[1] studied the velocity field in a small-size cylindrical cyclone; Hoekstra et al.[2,3] measured the flow field in a cyclone of industrial dimensions. Derksen and Van den Akker[4]found that Reynolds stress model (RSM) fluctuation velocities near the center are much higher than those close to the wall; Lu et al.[5] measured the Reynolds stresses in a liquid–liquid hydrocyclone and reported that the turbulence is anisotropic. All of these studies were done only for the separation space, whereas the flow field in the dust hopper and annular space are less studied. For numerical simulation, Boysan et al.[6] first simulated the 2-D turbulent flows in a cyclone using an algebraic stress model (ASM).

Predictions give the pressure drop vs. as the flow rate in agreement with the experimental results, but the predicted velocities and Reynolds stresses are not verified by measurements. Zhou and Soo[7] predicted time-averaged axial and tangential velocities and the pressure distribution using the k–ε model, which are near to their laser Doppler velocimetry (LDV) measurement results. The above-stated simulation studies were done only for the separation space. Hoffman et al.[8]

Correspondence concerning this article should be addressed to L. Y. Hu at huliyuan@mail.tsinghua.edu.cn.

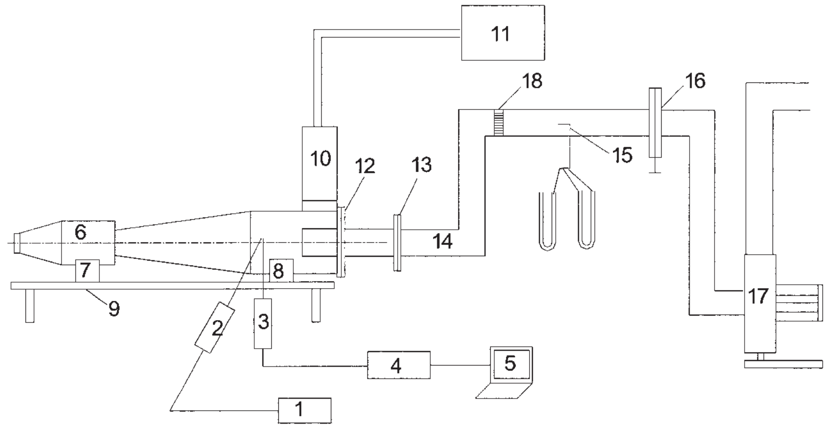

Figure 1. Experimental setup.

1. laser; 2. emitter unit; 3. receiver; 4. signal processor; 5. data processor; 6. cyclone; 7. 8. wood block; 9. steel table; 10. inlet tube; 11. smog feeder; 12. 13. flange; 14. outlet pipe; 15. pitot tube; 16. valve; 17. fan; 18. stabilizer.

studied the effect of the dust hopper on the flow field in a cyclone using the ASM model and found that the hopper has a significant influence on the flow field. Meier and Mori[9] used an anisotropic k–ε model and reported that there are recirculation zones near and within the dust hopper. Lu et al.[10] simulated turbulent flows in hydrocyclones using the k–ε, renormalization group (RNG) k–ε, and RSM models. It is found that only the prediction results using the RSM model are near to LDV measurement results. Derksen and Van den Akker[4] investigated large-eddy simulation (LES) to give the time-averaged and RSM velocities in good agreement with the experimental results. The simulation shows the vortex core precession and a shortcut flow at the bottom of the vortex finder, which is enhanced by the longitudinal recirculation in the annular space. Peng[11], using a hybrid ASM–RSM model, showed that a shortcut flow exists at the bottom of the vortex finder and the solid-body rotation zone (vortex core) is asymmetric. In summary, it is recognized that only the Reynolds stress model is appropriate for simulating strongly swirling flows in cyclones and, even so, only the predicted time-mean velocities are reasonable, although for Reynolds stresses the agreement between predictions and measurements is poor. Most investigators neglect the effect of the dust hoppers and the annular space.

In this article, the 3-D strongly swirling turbulent flows in the full space of a cyclone separator are measured by LDV, and are simulated using a Reynolds stress model by improving the empirical constants in the pressure–strain term of the Reynolds stress equation incorporated into the platform of FLUENT 6.0.

It should be pointed out that as a first step of our research, only the gas flow field is studied herein because the effect of particles on the gas flow field is negligible, whereas the effect of gas flow field on the particle motion is significant. The motion of particles will be studied later.

Experimental Setup and Measurement Methods

The experimental setup, shown in Figure 1, consists of an air draft system, measurement system, and a cyclone model. The air is exhausted through the outlet tube, or vortex finder, at the top of the cyclone. The air flow rate is controlled by a knife switch in the outlet pipe and a Pitot tube. The cyclone model is made of transparent, acrylic plastic with a diameter of 250 mm. The inlet tube has a rectangular cross section of 122 mm height and 63 mm width. The swirl numbers are 2.810 and 2.018, corresponding to vortex finder diameters of 110 and 79 mm, respectively. The air inlet velocities are 7.2, 9, 11.2, and 14 m/s. On one side and the top of the cyclone model, several slots are opened and some pieces of optical glass are mounted to avoid laser interference.

A 3-D LDV with a backward-scattering arrangement, made by TSI Inc., was used to measure the flow field in the cyclone. Tracer particles are glycol droplets of 5 μm, provided by a LZL-II particle producer. Measuring cross sections are shown in Figure 2. Measurements were taken every 5 mm in the radial direction except in the vicinity of the wall where the radial increment is 1 mm. Under the vortex finder, the axial increments of the measuring cross sections vary from 30 to 40 mm, except that the axial increment is 10 mm near the sudden-expansion section. In the annular space, the axial increment is 10 mm near the bottom of the vortex finder, 1–5 mm near the top, and 20 mm in most of the space. When flows in the separation space and the dust hopper are measured, the axis of the cyclone is normal to the axis of the converging beams, and tangential and axial velocities could be measured. When flows in the annular space is measured, the axis of the cyclone is parallel to the axis of the converging beams, tangential and radial velocities could be measured, and the smallest distance between the measuring location and the wall of the cyclone or vortex finder is 10 mm. When the flow field in the cone is measured, the measuring cross sections of the cone are parallel to that of the cylinder by moving the coordinate system because the axis of the converging beams must be normal to the optical glass. For each measuring location, the distance that the coordinate system moves in the x-axis is $dx = a \cos \theta$, and is $dy = a \sin \theta$ in the y-axis. The converging beams thus focus on the line AB.

Mathematical Model and Numerical Method

When using the Reynolds stress turbulence model, beside the momentum and continuity equations, the transport equations of Reynolds stresses can be written as

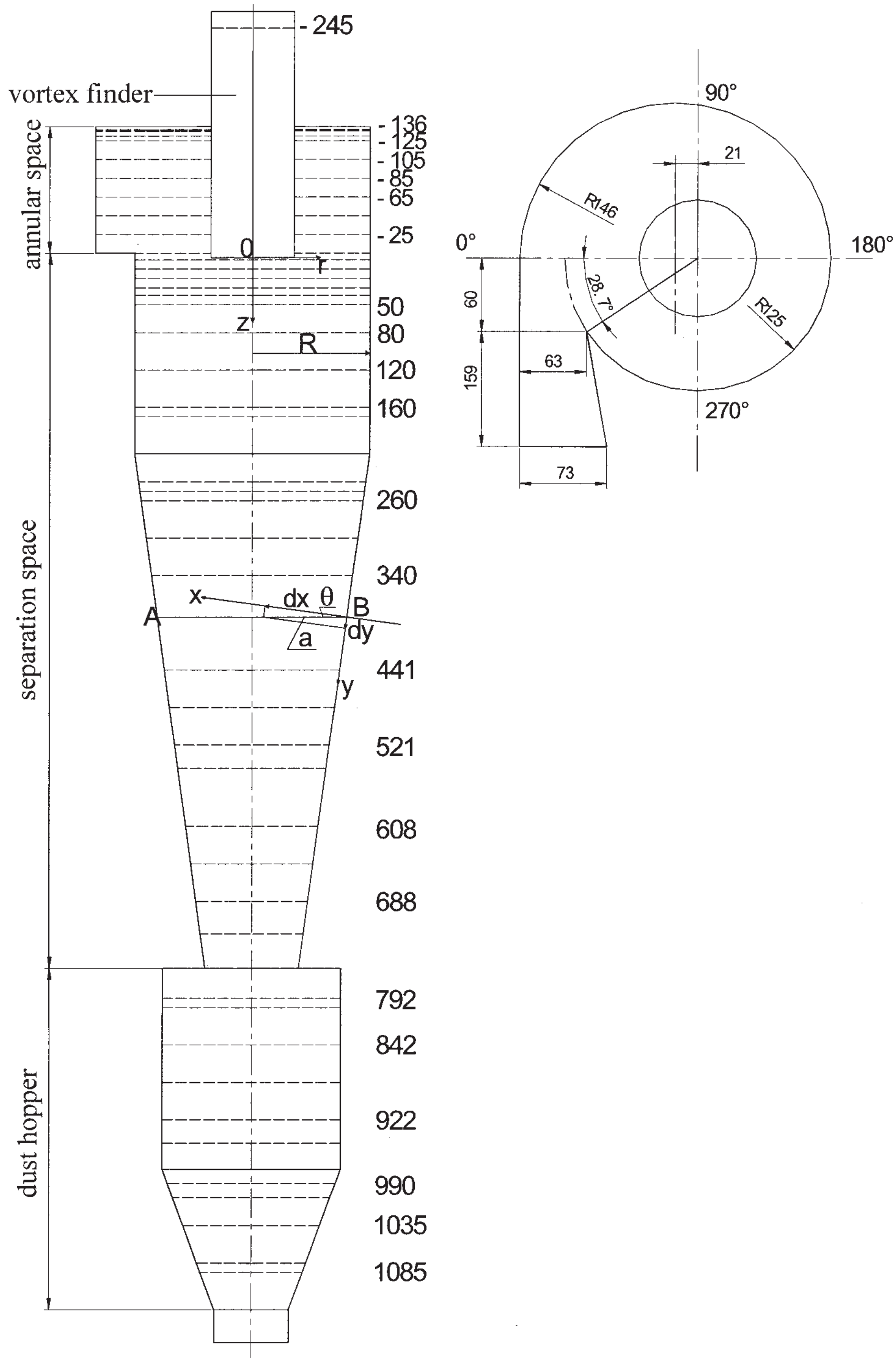

Figure 2. Measuring cross sections and the top view of the annular space.

$$\frac{\partial}{\partial t}(\rho \overline{u_i u_j}) + \frac{\partial}{\partial x_k}(\rho U_k \overline{u_i u_j}) = D_{ij} + P_{ij} + \Pi_{ij} - \varepsilon_{ij} \quad (1)$$

where the four terms on the righthand side stand for stress diffusion, stress production, pressure strain, and dissipation terms, respectively. Of these terms, P_{ij} does not require any modeling. The closure models for D_{ij} and ε_{ij} are the Daly–Harlow model and an isotropic dissipation model, respectively:

$$D_{T,ij} = -\frac{\partial}{\partial x_k}\left[c_s \rho \frac{k}{\varepsilon} \overline{u_k u_l} \frac{\partial}{\partial x_l}(\overline{u_i u_j})\right] \qquad \varepsilon_{ij} = \frac{2}{3}\delta_{ij}\rho\varepsilon \quad (2)$$

The closure model of the pressure–strain term Π_{ij} is most important in predicting Reynolds stresses. There are linear and nonlinear pressure–strain models such as IPM, IPCM, GL, SSG, and FLT models. The empirical constants in the IPCM (isotropization of production and convection model) + wall (the wall-reflection term) pressure–strain model are modified for simulating strongly swirling turbulent flows. The physical meaning of Π_{ij} is turbulence redistribution, decomposed into three parts

$$\Pi_{ij} = \Pi_{ij1} + \Pi_{ij2} + \Pi_{ij3} \tag{3}$$

$$\Pi_{ij1} = -C_1\rho \frac{\varepsilon}{k}\left[\overline{u_i u_j} - \frac{2}{3}\delta_{ij}k\right] \tag{4}$$

$$\Pi_{ij2} = -C_2\left[(P_{ij} - C_{ij}) - \frac{1}{3}\delta_{ij}(P_{kk} - C_{kk})\right] \tag{5}$$

$$\Pi_{ij3} = C_1' \frac{\varepsilon}{k}\left(\overline{u_k u_m} n_k n_m \delta_{ij} - \frac{3}{2}\overline{u_i u_k} n_j n_k - \frac{3}{2}\overline{u_j u_k} n_i n_k\right)\frac{k^{3/2}}{C_l \varepsilon d} + C_2'\left(\Pi_{km,2} n_k n_m \delta_{ij} - \frac{3}{2}\Pi_{ik,2} n_j n_k - \frac{3}{2}\Pi_{jk,2} n_i n_k\right)\frac{k^{3/2}}{C_l \varepsilon d} \tag{6}$$

where Π_{ij1} is a slow pressure–strain term, reflecting the turbulence–turbulence interaction, also known as the return-to-isotropy term; Π_{ij2} is called the rapid pressure–strain term, or a turbulence-mean flow interaction term, reflecting the influence of mean flows on the turbulence field; and Π_{ij3} is the wall-reflection term. The slow term has the effect of isotropizing the turbulent fluctuation. The rapid term has the effect of isotropizing the production and convection processes. The wall-reflection term Π_{ij3} is responsible for the redistribution of normal stresses near the wall. It tends to damp the normal stress perpendicular to the wall, while enhancing the stresses parallel to the wall; $k = (1/2)\overline{u_i u_i}$; $C_l = C_\mu^{3/4}/\kappa$; n_i is the i component normal to the wall; C_1, C_2, C_1', C_2', $C_{\varepsilon 1}$, $C_{\varepsilon 2}$, C_μ, and κ are model constants ($\kappa = 0.4187$); k is the turbulent kinetic energy; δ_{ij} is the Kronecker delta; and d is the normal distance to the wall.

Nikjooy and Mongia[12] indicate that the inability of the second-moment closure to correctly resolve the turbulence field could be attributed, to a large extent, to the modeling of the Π_{ij} term. For swirling flows, the redistribution of turbulence by fluctuating pressure is different from that for nonswirling flows. A vast range of values has been suggested for C_1 and C_2 by different researchers. Most choices of C_1 and C_2 are $(1 - C_2)/C_1 = 0.23$.[13] The original work of Naot et al.[14] neglected the return-to-isotropy process (Π_{ij1}) and proposed a large value of $C_2 = 0.6$ for the Π_{ij2} model constant. Conversely, Donaldson's proposal[15] totally ignored the Π_{ij2} process and just included a contribution from the Π_{ij1} process, with a large model constant of $C_1 = 5$. Gibson and Younis[16] proposed a simple modification of model constants, $C_1 = 3.0$ and $C_2 = 0.3$, a choice that emphasizes Π_{ij1} more than Π_{ij2}. This choice is based on the observation that swirling flows are better predicted with this combination. Nikjooy examined three options for C_1 and C_2, and found that for the case of $C_2 = 0$ the results are insensitive to C_1, but when $C_2 \neq 0$ the combination of C_1 and C_2 is important. The above-suggested values of C_1 and C_2 are not suitable for strongly swirling flows in cyclones by the numerical experiments made by the present authors. The Reynolds stress equation model is improved by modifying the empirical constants in the IPCM + wall pressure–strain term. The standard and modified empirical constants for strongly swirling flows are shown in Table 1. For the modified constants $C_2 = 0$ means that, for strongly swirling flows in cyclones, only the isotropization of Reynolds stresses is important and the effect of isotropization of the production and convection processes is very small and can be neglected.

Table 1. Empirical Constants in IPCM + Wall Model

Empirical Constant	$C_{\varepsilon 1}$	$C_{\varepsilon 2}$	C_1	C_2	C_1'	C_2'	C_μ
Standard	1.44	1.92	1.8	0.6	0.5	0.3	0.09
Modified	1.66	1.92	130	0	150	0.3	0.09

The scalar dissipation rate ε is determined by the following transport equation

$$\frac{\partial}{\partial t}(\rho\varepsilon) + \frac{\partial}{\partial x_i}(\rho\varepsilon u_i) = \frac{\partial}{\partial x_j}\left[\left(\mu + \frac{\mu_t}{\sigma_\varepsilon}\right)\frac{\partial \varepsilon}{\partial x_j}\right] + C_{\varepsilon 1}\frac{1}{2}P_{ii}\frac{\varepsilon}{k} - C_{\varepsilon 2}\rho\frac{\varepsilon^2}{k} \tag{7}$$

A cyclone model with the vortex finder of 79 mm diameter is simulated. The inlet velocity components according to the experimental parameters are $V_z = 0$ m/s, $V_r = 0$ m/s, $V_t = 14$ m/s; $k = (3/2)(u_{avg}I)^2 = 0.735$ m^2/s^2, $(u_i u_j)_{in} = (2/3)k_{in} = 0.49$ m^2/s^2, $\overline{u_i' u_j'} = 0$ m^2/s^2, $\varepsilon = c_\mu^{0.75}k^{1.5}/l = 17.021$ m^2/s^3, where $C_\mu = 0.09$, $\kappa = 1.42$, $D_H = 0.0869$ m, u_{avg} is the average velocity at the inlet, k is the turbulent kinetic energy, l is the turbulent length scale ($l = 0.07D_H$), and I is the turbulent intensity ($I = 0.05$). The boundary condition at the exit is based on a fully developed flow assumption where the gradients for all flow variables in the axial direction are zero, that is, $\partial\varphi/\partial Z = 0$. In computation the outlet pipe of the cyclone is lengthened to meet this assumption. The standard wall function approximation is adopted for near-wall grid nodes. Near-wall grid spacing is about 5 mm. The number of grids is 101,450. The flow field does not change when the number of grid nodes increases, so this number is sufficient for a grid independent solution. Most of the mesh type is hexagon. The above-stated model is incorporated into the platform of FLUENT 6.0. The QUICK difference scheme for the convection and diffusion terms is adopted and the finite-difference equations are solved using the SIMPLE algorithm.

Results and Discussion

The separation space

Figure 3 shows the measured and predicted tangential velocities. The tangential velocity distribution shows the typical feature of strongly swirling flows: a Rankine-vortex structure with good symmetry. The predicted tangential velocities are in agreement with the measurement results.

The position and the value of the maximum tangential velocities are basically independent of the axial locations, but depend only on the diameter of the vortex finder, indicating that swirl does not attenuate in the separation space. The time-averaged tangential velocities near the wall are still very large at a distance of 1 mm, which implies that the thickness of the boundary layer is <1 mm. Figure 4 gives the measured and

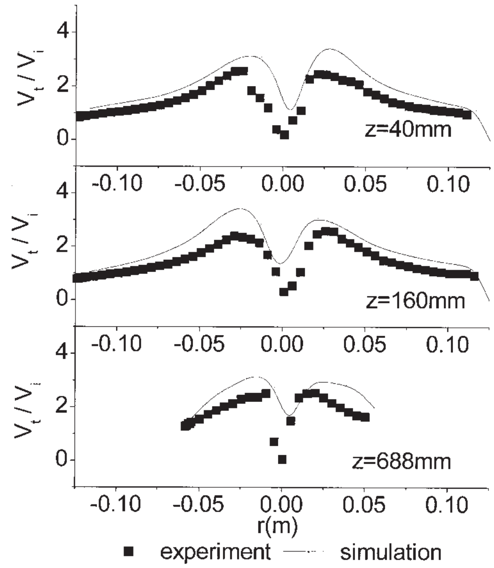

Figure 3. Tangential velocity in the separation space.

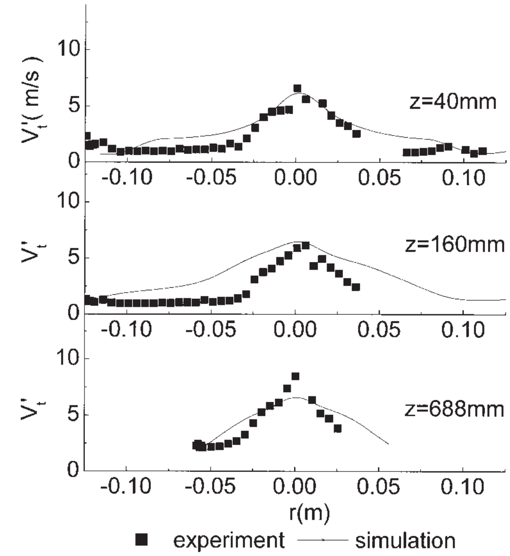

Figure 5. Tangential RSM velocity in the separation space.

predicted time-averaged axial velocity profiles. Good agreement is obtained between predictions and measurements. The axial velocity distribution with good symmetry consists of an upward-flow zone and a downward-flow zone. The magnitude of the axial velocity in the upward-flow zone is of the same order of magnitude as that of the inlet velocity, and in the downward-flow zone is smaller than the inlet velocity by an order of magnitude. The area of the upward-flow is one third that of the cross section in most of the separation space, but is about half that near the discharge port. The recirculation near the axis and the inlet of the vortex finder may result from the increase of the average pressure in the vortex finder with the increase of the diameter of the vortex finder. In the cone section the axial velocity profiles of upward flows still show one peak and the maximum axial velocities are close to the inlet velocity. In the cylindrical section, the intersection point between upward flows and downward flows is independent of the axial position. In the cone section, it gradually shifts inward along the axial direction and shows a cone shape.

Figures 5 and 6 show the measured and predicted tangential and axial RSM fluctuation velocities, respectively, in the separation space. The predicted RSM velocities agree well with the measurement results. The axial RSM velocity profiles and the tangential RSM velocity profiles are in a similar form. The maximum tangential RSM velocity is larger than the axial RSM velocity, the maximum axial RSM velocity near the centerline is about 3.78 m/s, and the maximum tangential RSM velocity varies from 3.78 to 5.6 m/s, showing an anisotropic turbulence in strongly swirling flows, although they are generally of the same order of magnitude. The shapes of RSM velocity profiles are different in different regions. In the upper

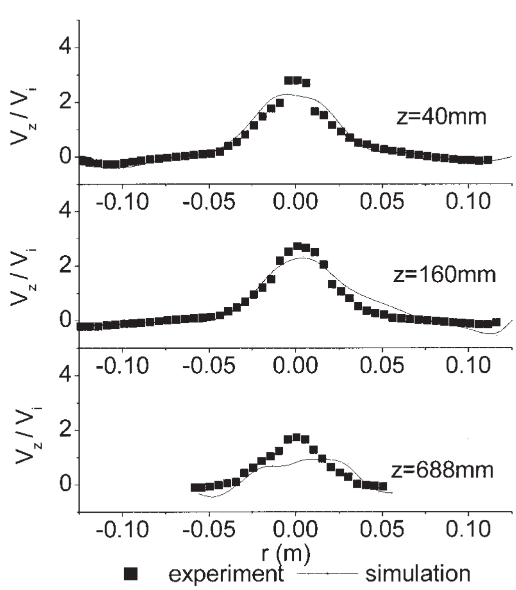

Figure 4. Axial velocity in the separation space.

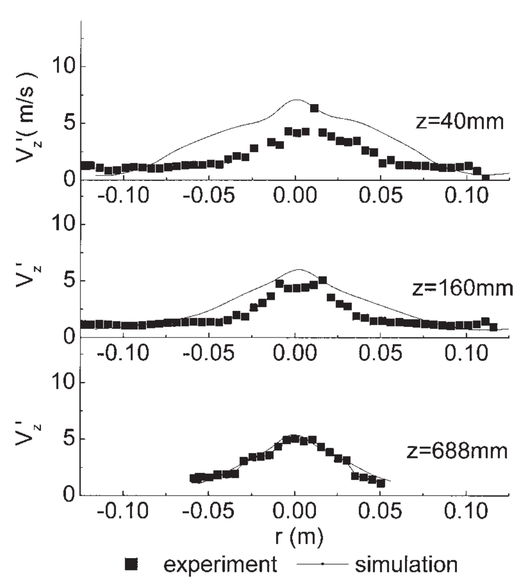

Figure 6. Axial RSM velocity in the separation space.

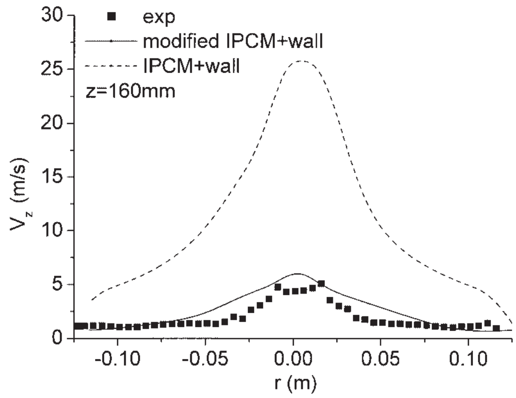

Figure 7. Axial RSM velocity predicted using the modified and standard IPCM + wall models.

region, especially in the cylindrical section, the RSM velocities are almost independent of the axial positions, approximately unchanged in the outer vortex flows, and increase with the decrease of the radial distance in inner vortex flows. Near the wall, the tangential RSM velocities increase sharply. In the lower region, that is, the entrainment region near the discharge port, the RSM velocities increase with the decrease of the radial distance in the whole cross section.

Figure 7 shows the comparison of the axial RSM velocity distribution at z = 160 mm using the modified IPCM + wall model and the standard IPCM + wall model. The results indicate that the predicted axial RSM velocity using the modified IPCM + wall model are much better than that obtained using the standard IPCM + wall model.

The annular space

The geometrical configuration of the annular space shown in Figure 2 is nonaxisymmetric. Sixteen cross sections are measured in 0, 180, and 270° azimuth, respectively. The time-averaged tangential velocity profiles are shown in Figure 8. The predicted tangential velocities agree well with the measurement results. The y-axis is taken as the outer wall of the vortex finder. Figure 8 indicates that the time-averaged tangential velocity increases gradually with the decrease of the radius, and is more uniform than that in the separation space. The distribution is a quasi-free vortex except near the wall of the vortex finder. It begins to decrease near the wall at a distance of 3–4 mm (see Figure 8c), indicating that the velocity gradients are large, forming a shear layer. The velocity profiles at various axial positions are almost the same. The velocity distribution is nonaxisymmetric in the annular space. The time-averaged tangential velocities in the 180° azimuth are obviously higher than that in 0 and 270° azimuths. They increase gradually from 0 to 180° and decrease gradually from 180 to 270°. The time-averaged tangential velocities are accelerated

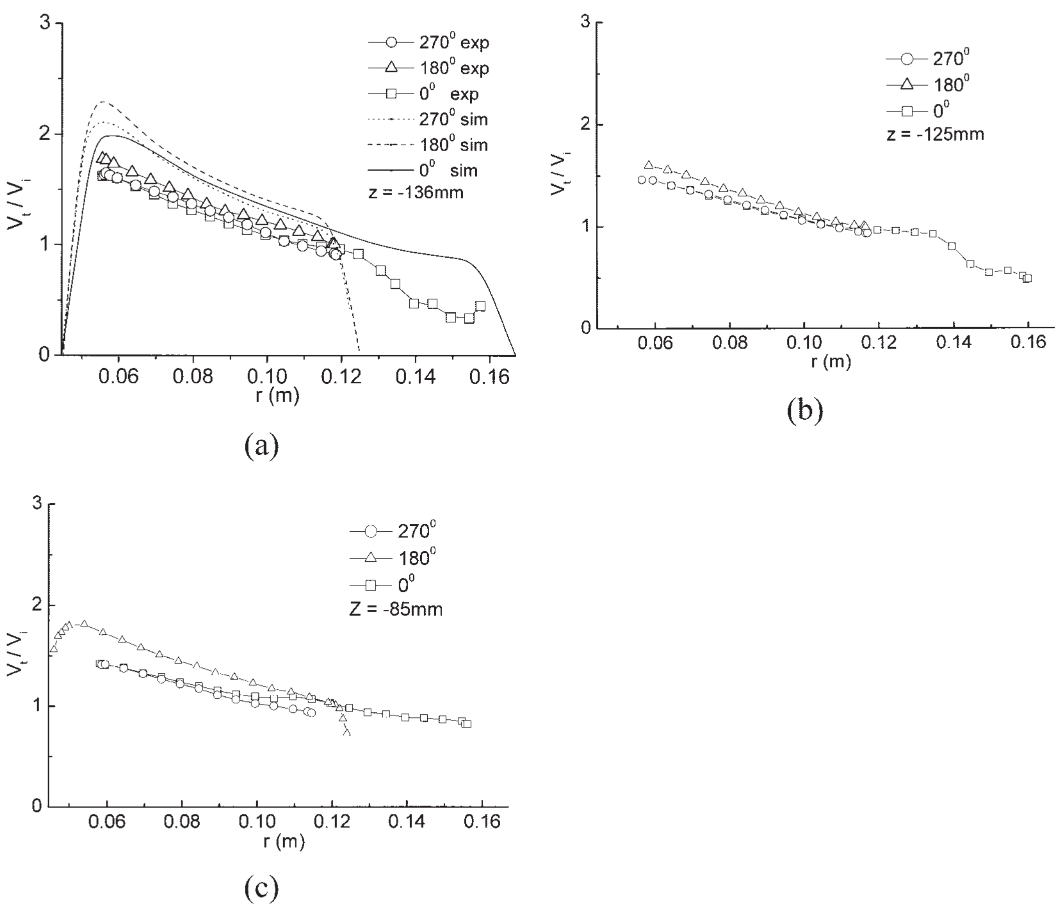

Figure 8. Tangential velocity in three azimuths.

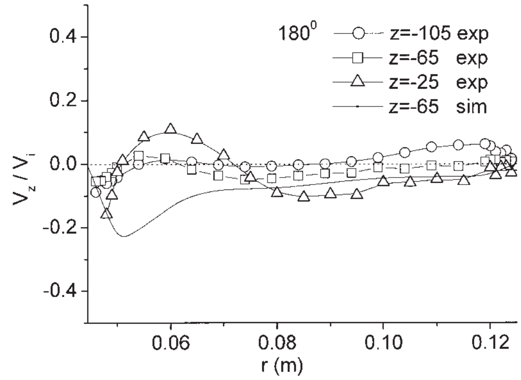

Figure 9. Axial velocity at 180°.

because the radial width of the annular space in a volute cyclone is reduced from 0 to 180°, and decelerated because the gas flows gradually enter the separation space, whereas the radial width is fixed from 180 to 360°. In the 0° azimuth, when $r > R$, the tangential velocity decreases sharply and it is very low near the wall in the upper region. In the lower region, it is more uniform than that in the upper region and it is high near the wall. In the 180° azimuth, the maximum dimensionless tangential velocity (see Figure 8c) is about 1.81 and is smaller than that in the separation space. Its position is almost independent of the axial locations.

Figure 9 shows the time-averaged axial velocity distribution in the 180° azimuth. The axial velocity profiles in the annular space differ greatly from those in the separation space. The axial velocity is one order of magnitude smaller than the tangential velocity in the annular space. Near the bottom of the vortex finder, the axial velocity profile shows an upward flow near the wall of the vortex finder, and a downward flow near the wall of the cyclone. Above the cross section $z = -65$ mm, the flows are almost downward, but near the top, such as at the cross section $z = -105$ mm, the axial velocity profile shows an upward flow near the wall of the cyclone. Figure 9 still shows the predicted axial velocity distribution at $z = -85$ mm in the 180° azimuth in good agreement with the measurements results.

The predicted and measured radial velocities are centripetal in most of the cross sections near the top of the cyclone except in the 0° azimuth. In Figure 10 the predicted velocity vectors show that there is a secondary longitudinal vortex of 5–6 mm height near the top of the cyclone, which is harmful to dust separation.

Figure 11 shows the axial RSM velocity profiles in the 180° azimuth. It can be seen that the axial RSM velocity profiles at various axial positions are almost the same. The axial RSM velocity increases slightly with increasing radial distance. The value of the axial RSM velocity in the annular space is close to that in the outer vortex flow in the separation space. The axial RSM velocity is very large where the axial velocity gradient is very large near the wall.

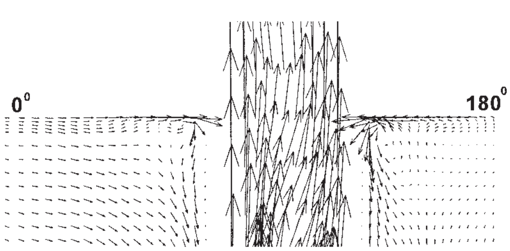

Figure 10. Velocity vectors near the top of the cyclone.

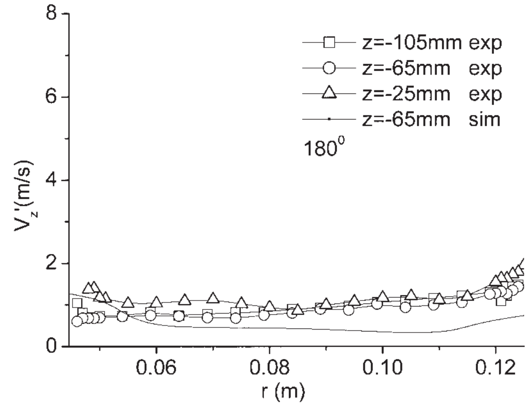

Figure 11. Axial RSM velocity in the 180° azimuth.

The tangential RSM velocity, like the time-averaged tangential velocity, is almost independent of axial positions in this azimuth. The tangential RSM velocities, like the axial RSM velocities, vary smoothly in most regions, but increase sharply near the walls (Figure 12). In Figure 12, the *y*-axis is taken as the outer wall of the vortex finder. The magnitude of the tangential RSM velocity is of the same order of magnitude as that in the outer vortex flow in the separation space, but is lower. The tangential RSM velocity varies greatly along the peripheral direction (Figure 12) and is nonaxisymmetric. It is the largest in the 0° azimuth where the fresh inlet air is mixed with the air that has rotated in the annular space, and is the smallest in the 270° azimuth. It seems that the tangential RSM velocity decreases along the peripheral direction clockwise. Both predictions and experiments show that the magnitudes of three RSM velocity components in the annular space are of the same order of magnitude.

The dust hopper

Six cross sections were measured in the cylindrical section and five cross sections were measured in the cone section in the

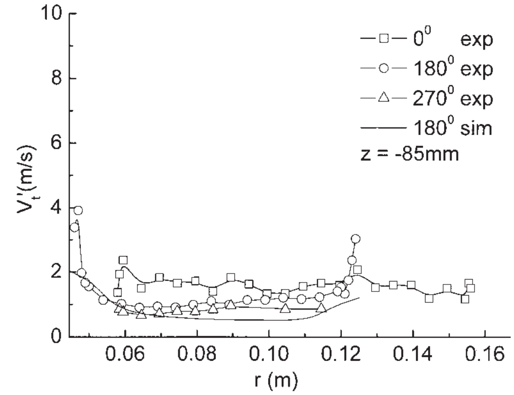

Figure 12. Tangential RSM velocity along the azimuthal direction.

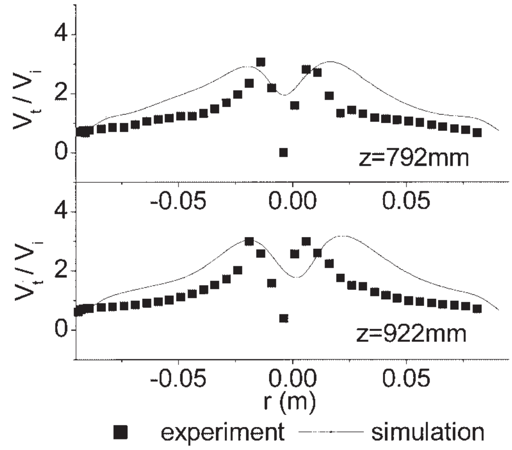

Figure 13. Tangential velocity in the dust hopper.

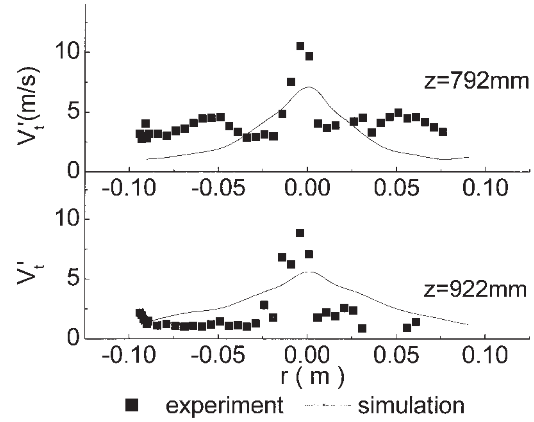

Figure 15. Tangential RSM velocity in the dust hopper.

dust hopper. Figures 13 to 16 give the predicted and measured tangential and axial time-averaged and RSM velocity profiles. The agreement between predictions and measurements are fairly good. The axisymmetric tangential velocity distribution in the dust hopper is similar to that in the separation space. The maximum tangential velocity in the dust hopper is higher than that in the separation space because of the sudden reduction of the space. The swirling flows are still sufficiently strong. The position of the maximum tangential velocities in the cylindrical section is almost independent of the axial locations and the diameter of the vortex finder and depends on the diameter of the discharge port. In the cone section, it gradually shifts inward along the axial direction. The value of the maximum tangential velocity is independent of the axial locations.

The time-averaged axial velocity distribution in the dust hopper differs from that in the separation space. Both predictions and experiments show that a weak upward flow exists near the wall at the top and, with the decrease of the radial distance, the flow turns downward at first, then upward. That is, a secondary longitudinal vortex with a height of about 30 mm exists near the top of the dust hopper, which is clearly shown by the velocity vectors given in the simulated results (Figure 17). This indicates that the separation efficiency will be improved if the structure of the dust hopper can be improved.

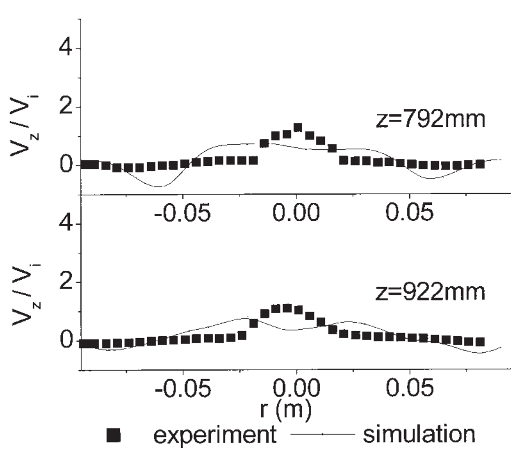

Figure 14. Axial velocity in the dust hopper.

The vortex finder

Figure 18 shows the time-averaged tangential and axial velocity and RSM velocity profiles at one axial position for d_r = 79 mm. The simulated values are larger than the measured values. The flows are axisymmetric. Both predictions and experiments show Rankine-vortex tangential velocity profiles in the vortex finder, but the size of the inner vortex is larger than that in the separation space and is half the diameter of the vortex finder. The experimental maximum dimensionless tangential velocity is 2.3 and is lower than that in the separation space. The experimental dimensionless tangential velocity near the wall is 1.66 and is larger than that in the separation space. This implies that the swirling flows in the vortex finder do not attenuate sharply, which is a main factor causing the pressure drop in the cyclone.

The axial velocity distribution is much different from that in the separation space. It is very small in the geometrical center of swirling flows, increases sharply with the increase of radial distance, and somewhat decreases near the wall. The experimental maximum dimensionless axial velocity is about 1.7 and is somewhat lower than that in the separation space. The flows are thus mainly near the wall.

Both predictions and experiments show that the RSM velocities are still large, they are high near the axis and low near the wall, and the tangential RSM velocity is higher than the axial RSM velocity, indicating that the turbulence is still anisotropic in the vortex finder.

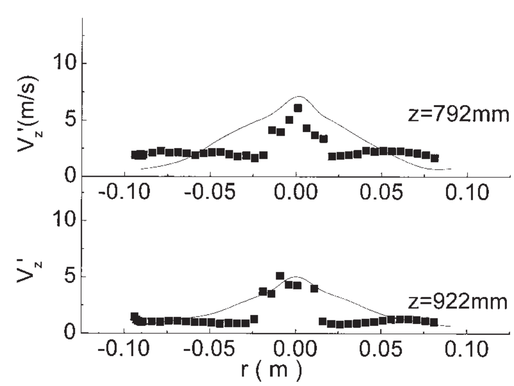

Figure 16. Axial RSM velocity in the dust hopper.

Conclusions

(1) The strongly swirling flows in a cyclone show structures of a Rankine vortex, inner downward flows, and outer upward flows.

(2) In outer-vortex flows of the separation space, the tangential and axial RSM velocities are small and change slightly along radial and axial directions. In inner-vortex flows they are large and change substantially along the radial direction. At the intersection points between upward flows and downward flows, the axial turbulence intensity is rather high. The RSM velocities and the turbulence intensities are also quite large near the discharge port.

(3) In the annular space, the magnitudes of three RSM velocity components are of the same order. The RSM velocities are the largest in the 0° azimuth, the smallest in the 270° azimuth, and tend to decrease along the peripheral direction clockwise. At the entrance, near the wall and the top, the RSM velocities are very large and show anisotropic turbulence.

(4) A secondary longitudinal vortex of 30 mm height exists near the top of the dust hopper and that of 5–6 mm exists near the top of the cyclone.

(5) In the vortex finder the axial velocity distribution is quite different from that in the separation space. The axial velocity is very small in the geometrical center of swirling flows, increases sharply with the increase of the radial distance, and decreases near the wall. The tangential velocity distribution also shows a Rankine-vortex structure, but the size of the inner vortex is larger. The turbulence is still anisotropic in the vortex finder.

(6) The predicted tangential and axial velocities, especially the tangential and axial RSM velocities using the Reynolds stress model with modified coefficients in the IPCM + wall model of the pressure–strain term are more reasonable than those previously reported. Predictions in the full space of a cyclone are obtained for the first time.

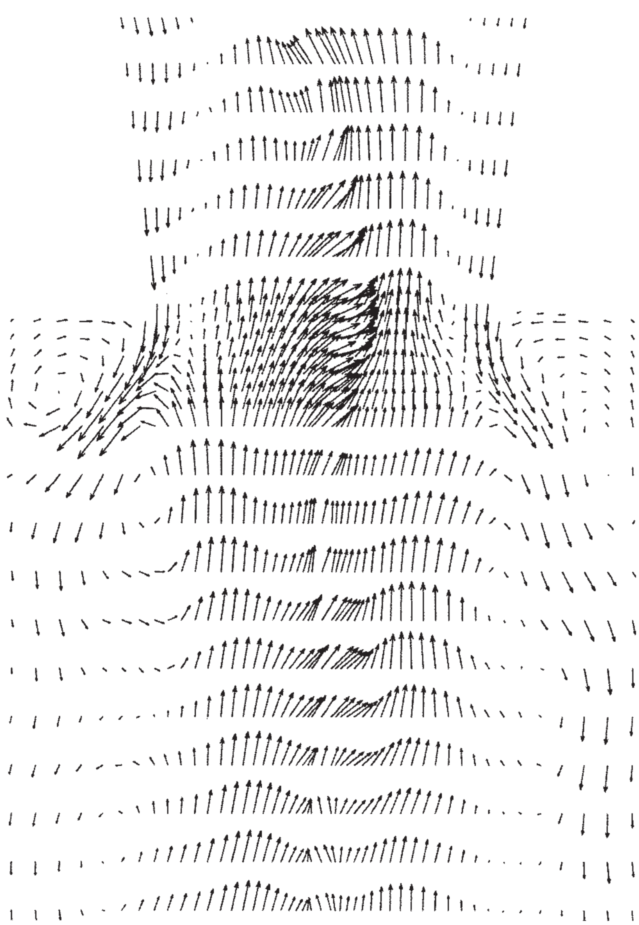

Figure 17. Velocity vectors near the top of the dust hopper.

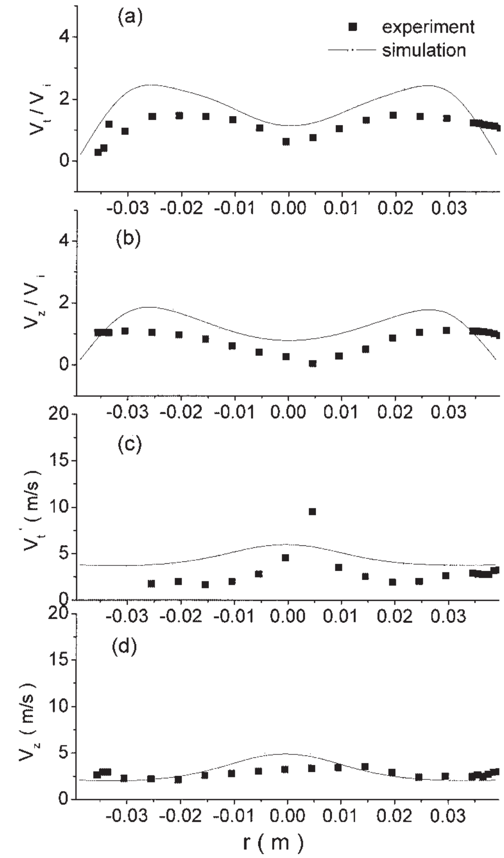

Figure 18. Tangential and axial velocities and RSM velocities in the vortex finder.

Notation

d_r = diameter of the vortex finder, mm
R = radius of the cyclone, mm
r = radial distance, mm
V_i = inlet velocity, m/s
V_t = tangential velocity, m/s
V_z = axial velocity, m/s
V'_z = axial RSM velocity, m/s
V'_t = tangential RSM velocity, m/s
Z = axial coordinate, mm
θ = semicone angle

Literature Cited

1. DeOtte RE Jr. Characterization of the velocity field in a small, cylindrical, low Reynolds number aerosol sampling cyclone. *Aerosol Sci Technol.* 1990;12:1037-1049.
2. Hoekstra AJ, Derksen JJ, Van den Akker HEA. An experimental and

numerical study of turbulent swirling flow in gas cyclones. *Chem Eng Sci*. 1999;54:2055-2065.
3. Hoekstra AJ, Van Vliet E, Derksen JJ, Van den Akker HEA. Vortex core precession in a gas cyclone. *Advances in Turbulence VII*. Dordrecht, Netherlands: Kluwer Academic; 1998:289-292.
4. Derksen JJ, Van den Akker HEA. Simulation of vortex core precession in a reverse-flow cyclone. *AIChE J*. 2000;46:1317-1331.
5. Lu Y-J, Shen X, Zhou L-X. LDV diagnosis for the flow field in a liquid–liquid hydrocyclone with double cones and cylinders. *J Exp Mech* (*China*). 1999;14:452-463.
6. Boysan F, Ayers W, Swithenbank J. Fundamental mathematical modeling approach to cyclone design. *Trans Inst Chem Eng*. 1982;60:222-230.
7. Zhou LX, Soo SL. Gas–solid flow and collection of solids in a cyclone separator. *Powder Technol*. 1990;63:45-53.
8. Hoffman AC, de Groot M, Hospers A. The effect of the dust collection system on the flow pattern and separation efficiency of a gas cyclone. *Can J Chem Eng*. 1996;74:464-470.
9. Meier HF, Mori M. Anisotropic behavior of the Reynolds stress in gas and gas–solid flows in cyclones. *Powder Technol*. 1999;101:108-119.
10. Lu Y-J, Shen X, Zhou L-X. Application and comparison of different turbulence models in simulating liquid–liquid hydrocyclones. *J Tsinguha Univ* (*China*). 2001;41:105-109.
11. Peng W-M. Numerical simulation and experimental studies on the flow field in a cyclone separator. *J Agric Machines* (*China*). 2001;32:20-24.
12. Nikjooy M, Mongia HC. A second-order modeling study of confined swirling flow. *Int J Heat Fluid Flow*. 1991;12:12-19.
13. Launder BE. Second-moment closure and its use in modeling turbulent industrial flows. *Int J Numer Methods Fluids*. 1989;9:963-985.
14. Naot D, Shavit A, Wolfshtein M. Interactions between components of the turbulent velocity correlation tensor. *Israel J Technol*. 1970;8:259-269.
15. Donaldson CP. A computer study of boundary layer transition. *AIAA J*. 1969;7:271.
16. Gibson MM, Younis AB. Calculation of swirling jets with a Reynolds stress closure. *Phys Fluids*. 1986;29:38-48.

Manuscript received Nov. 19, 2003, and revision received July 9, 2004.